Towards compact and snapshot channeled Mueller matrix imaging

Aun Zaidi[1,2,*], Scott McEldowney[1], Yun-Han Lee[1], Qing Chao[1], and Lu Lu[1]

[1] *Facebook Reality Labs, Redmond, Washington 98052, USA*
[2] *Harvard John A. Paulson School of Engineering and Applied Sciences, Harvard University, Cambridge, MA 02138, USA*
[*] *Corresponding author: zaidi01@g.harvard.edu*

Compiled December 10, 2021

A polarization transformation can be fully described by a 4×4 matrix, known as the Mueller matrix. To fully image an object's polarization response, one needs to compute the Mueller matrix at each pixel of the image. Standard divison-of-time Mueller matrix imaging, because of its sequential nature, is ill-suited to applications requiring immediate and real-time imaging, and is also bulky due to multiple moving parts. In this work, we propose a new method for compact, snapshot Mueller matrix imaging, based on structured polarization illumination, and division-of-focal plane imaging, which can, in a single-shot, fully capture the Mueller matrix information of a band-limited signal.

http://dx.doi.org/10.1364/ao.XX.XXXXXX

Mueller matrix imaging (MMI) has long been a technique of interest in science and technology, because of its potential to reveal rich information about an object or material of interest [1]. A Mueller matrix encapsulates the entire polarization transforming property of an object, and can be used to extract out important physical parameters such as the depolarization index, diattenutation and retardance, to name a few [2]. There are two parts to MMI: the polarization state generator (PSG), and the polarization state analyzer (PSA). In the most common type of MMI technique – division-of-time (DoT) MMI – the object is sequentially illuminated with different polarization states generated by the PSG, and then sequentially analyzed by the PSA [3, 4]. If the PSA consists of an imaging system, then the Mueller matrix can be computed over the entire image, pixel by pixel, resulting in a Mueller matrix image. Even though, compared with other methods, DoT MMI systems are simpler to conceive and implement, they are ill-suited for applications requiring fast and/or real time response. Furthermore, DoT MMI systems often comprise of multiple moving parts, resulting in unwanted bulk. Some methods exist in which, the sequential PSA is replaced by a snapshot PSA, resulting in a hybrid MMI system that can improve the overall time resolution of the system [5, 6]. As opposed to DoT and hybrid MMI systems, a snapshot MMI system can retrieve all 16 spatially varying Mueller matrix components of a target at a single point in time, and is thus suitable for time sensitive applications. Solutions to designing a completely snapshot MMI system, however, have been few and far between, in comparison to DoT and hybrid MMI solutions. Furthermore, existing solutions to snapshot Mueller matrix imaging [7, 8] require multiple polarization gratings, waveplates and polarizers, adding to the bulk of the device and getting in the way of a compact implementation; apart from compactness, it is also desirable to reduce the number of components in an optical system to reduce complexity, avoid misalignment, and minimize aberrations. In this work, we propose a novel method to do snapshot Mueller matrix imaging, that can result in compact snapshot MMI systems, suitable for time-sensitive applications.

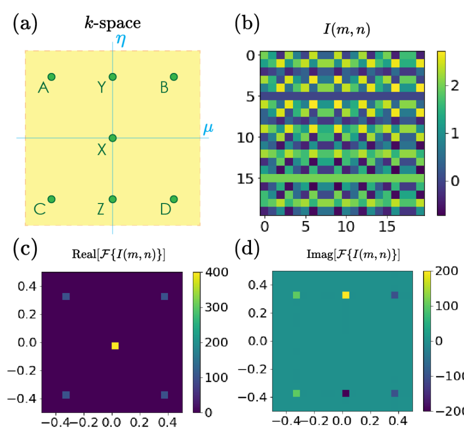

Fig. 1. DoFP Stokes Imaging Analysis. (a) A schematic of the 7 different spatial-frequency channels in k-space, labeled $\{A, B, C, D, X, Y, Z\}$. **(b)** $I(m,n)$ obtained when $\vec{S}(m,n) = [1\ 1\ 1\ 1]^T$ is analyzed by $\vec{S}_A$ in Eq.1, with $(a_A, b_A) = (0.7, 0.7)$. **(c)** The real part of the spatial spectrum of $I(m,n)$. **(d)** The imaginary part of the spatial spectrum of $I(m,n)$.

Let's first consider one-half of the MMI system: an imaging PSA. An imaging PSA is also known as a Stokes-camera. One of the most readily available type of compact Stokes-cameras, both in the lab and commercially, is the division-of-focal-plane (DoFP) Stokes-camera, in which grid polarizers are patterned directly on top of the sensor [9–11]. DoFP cameras are compact, snapshot, and thus suitable for compact time-sensitive applications. Another class of snapshot Stokes-cameras, known as division-of-amplitude (DoA) Stokes cameras also exist but, in comparison

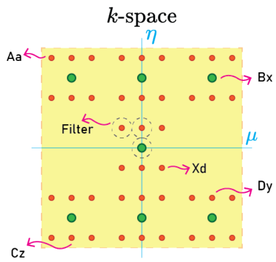

Fig. 2. Channels and Filtering in the Frequency Domain. The schematic shows the different spatial frequency channels plotted in *k*-space. Both the ‘main channels’ (green) introduced by the analyzer and the ‘sub-channels’ (orange) introduced by the illumination follow the same labeling convention as in Fig.1(a). Each channel is thus referred to by two letters, the capital letter referring to analyzer modulation and small letter referring to illumination modulation. Some examples have been labeled on the figure. An example of a possible low-pass filter (dotted line) is also shown in the figure.

to DoFP cameras, are less compact as they work by splitting the field into a minimum of four different channels or paths, which are then separately analyzed by polarizers [12]. Even though common DoFP Stokes-cameras usually only analyze for linear polarization states, recent advances in lithography techniques now allow for the direct patterning of waveplates on top of pixels, to analyze for arbitrary elliptical polarizations, resulting in compact full-Stokes imaging [13]. Now consider a custom designed DoFP full-Stokes camera whose analyzer Stokes vector $\vec{S}_A$ is a periodic function of discrete pixel coordinates (m,n):

$$\vec{S}_A(m,n) = \begin{pmatrix} 1 \\ cos(a_A m\pi)cos(b_A n\pi) \\ sin(a_A m\pi)cos(b_A n\pi) \\ sin(b_A n\pi) \end{pmatrix}, \quad (1)$$

where a_A, b_A control the spatial periodicity of the analyzer Stokes vector $\vec{S}_A(m,n)$. Let’s consider a general spatially varying incident Stokes vector: $\vec{S}(m,n) = [\, s_0(m,n) \;\; s_1(m,n) \;\; s_2(m,n) \;\; s_3(m,n)\,]^T$. Then, following analysis, the intensity pattern $I(m,n) = \vec{S}_A \cdot \vec{S}$ can be written as:

$$\begin{aligned} I(m,n) &= s_0(m,n) + s_1(m,n)cos(a_A m\pi)cos(b_A n\pi) \\ &+ s_2(m,n)sin(a_A m\pi)cos(b_A n\pi) + s_3(m,n)sin(b_A n\pi). \end{aligned} \quad (2)$$

As we see in Eq.2, different Stokes components of the incident field are being modulated with different 2D spatial harmonics. This maps the Stokes components of the incident field onto separate spatial-frequency channels in *k*-space, as shown in Fig1(a). The Stokes components can then be filtered in the Fourier domain, and retrieved by using a single snapshot intensity image $I(m,n)$. To visualize these channels in *k*-space, we consider the (unphysical) numerical example Stokes image $\vec{S}(m,n) = [1\ 1\ 1\ 1]^T$ to analyze, resulting in the intensity image $I(m,n)$ shown in Fig.1(b). As shown in Fig.1(c) and Fig.1(d), the discrete spatial frequency channels, illustrated in Fig1(a), are clearly visible, distributed across the real and imaginary parts of the spectra. Such methods have been explored previously in DoFP Stokes imaging, for both linear and full Stokes imaging [14]. In our work, we generalize such an approach to include both illumination and analysis, to allow the retrieval of all 16 spatially varying elements of a Mueller matrix in a snapshot way.

Now we consider the remaining half of an MMI system: PSG. To illuminate the object of interest, with multiple states of polarization at the same time, the PSG needs to generate a spatially varying Stokes illumination. Given recent advances, phase change platforms like liquid crystals and metasurfaces can be used to create desired patterns of structured polarization illumination with unprecedented resolution, using a compact, single element device [15, 16]. Now imagine we implement structured polarization illumination such that the Stokes vector of the 2D illumination varies periodically as:

$$\vec{S}_I(m,n) = \begin{pmatrix} 1 \\ cos(a_I m\pi)cos(b_I n\pi) \\ sin(a_I m\pi)cos(b_I n\pi) \\ sin(b_I n\pi) \end{pmatrix}, \quad (3)$$

where a_I, b_I control the spatial periodicity of the illumination Stokes vector $\vec{S}_I(m,n)$. Now let’s consider an object with polarization properties encapsulated by its spatially varying Mueller matrix:

$$\mathbf{M}_{obj}(m,n) = \begin{pmatrix} M_{00}(m,n) & M_{01}(m,n) & M_{02}(m,n) & M_{03}(m,n) \\ M_{10}(m,n) & M_{11}(m,n) & M_{12}(m,n) & M_{13}(m,n) \\ M_{20}(m,n) & M_{21}(m,n) & M_{22}(m,n) & M_{23}(m,n) \\ M_{30}(m,n) & M_{31}(m,n) & M_{32}(m,n) & M_{33}(m,n) \end{pmatrix}. \quad (4)$$

As the object (Eq.4) is illuminated with structured polarization (Eq.3), the spatially varying output Stokes vector, $\vec{S}_{out}(m,n)$ is given as:

$$\vec{S}_{out}(m,n) = \begin{pmatrix} M_{00} + M_{01}cos(a_I m\pi)cos(b_I n\pi) + M_{02}sin(a_I m\pi)cos(b_I n\pi) + M_{03}sin(b_I n\pi) \\ M_{10} + M_{11}cos(a_I m\pi)cos(b_I n\pi) + M_{12}sin(a_I m\pi)cos(b_I n\pi) + M_{13}sin(b_I n\pi) \\ M_{20} + M_{21}cos(a_I m\pi)cos(b_I n\pi) + M_{22}sin(a_I m\pi)cos(b_I n\pi) + M_{23}sin(b_I n\pi) \\ M_{30} + M_{31}cos(a_I m\pi)cos(b_I n\pi) + M_{32}sin(a_I m\pi)cos(b_I n\pi) + M_{33}sin(b_I n\pi) \end{pmatrix}. \quad (5)$$

(Note that in Eq.5, for Mueller components M_{00}, M_{01} etc, we have omitted the (m,n) dependence for brevity, even though they are, in general, spatially varying.) $\vec{S}_{out}(m,n)$ consists of four intensity images (as it is a 4 element/row spatially varying Stokes vector), where each intensity image has a form identical to Eq.2. We see in Eq.5 that the Mueller components of $\mathbf{M}_{obj}(m,n)$ are being mapped onto discrete spatial frequency channels due to the modulation introduced by the periodically structured polarization illumination. Now $\vec{S}_{out}$ needs to be analyzed in order to recover information about the Mueller matrix components. When $\vec{S}_{out}$ is analyzed by the DoFP Stokes camera of the form in Eq.1, the resulting, single intensity image $I(m,n)$ can be computed following Eq.2. It is intuitive to see what happens when a DoFP Stokes camera of the form in Eq.1 is used to analyze a signal $\vec{S}_{out}$ following structured illumination of the form in Eq.3: the analyzer places the resulting Stokes components of $\vec{S}_{out}$ in the 7 different frequency channels shown in Fig.1(a), where each of the 7 channels have been further split into 7 more channels (for a total of 49) due to the structured illumination. This is schematically shown in Fig.2. Thus, different components of the Mueller matrix get mapped onto different spatial frequency channels. Using simple linear equations shown in Table.1, we can filter and extract out the Mueller matrix components, and

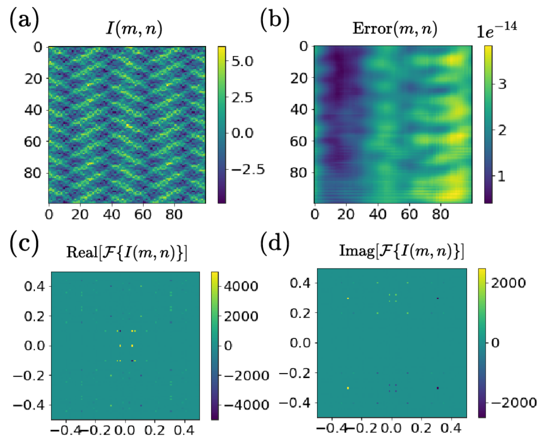

Fig. 3. A Numerical Example. We numerically test our method on the band-limited signal presented in Eq.6. **(a)** The resulting single-shot intensity image $I(m,n)$ used for processing. **(b)** The overall error (Eq.7) between the original and recovered Mueller matrix elements, as a function of lattice coordinates (m,n). **(c)** The real part of the spatial spectrum of $I(m,n)$. **(d)** The imaginary part of the spatial spectrum of $I(m,n)$.

can, theoretically, exactly recreate the original $\mathbf{M}_{obj}(m,n)$ if all the components of $\mathbf{M}_{obj}(m,n)$ are band limited, and their spatial spectra lie inside the radius of the filter.

As proof of concept, we numerically test our method on a band limited Mueller matrix signal. We use the parameters $(a_I, b_I) = (0.2, 0.2)$ for illumination, and $(a_A, b_A) = (0.6, 0.6)$ for analysis and a filter radius of 0.1 (in k-space). (The illumination parameters, in relation to analysis parameters, are chosen to be within the bound of the Nyquist criterion) .The Mueller matrix signal is defined on a 100×100, two-dimensional lattice as:

$$\mathbf{M}_{obj}(m,n) = \begin{pmatrix} cos(fm\pi) & 2cos(fm\pi) & sin(fm\pi) & 2sin(fm\pi) \\ cos(fn\pi) & 2cos(fn\pi) & sin(fn\pi) & 2sin(fn\pi) \\ 1 & sin(0.2fn\pi)cos(0.2fm\pi) & sin(0.2fn\pi)sin(0.2fm\pi) & cos(0.5fm\pi)sin(0.5fm\pi) \\ cos(0.2fn\pi)cos(0.2fm\pi) & 1 & 2 & sin(0.2fn\pi)sin(0.2fm\pi) \end{pmatrix}. \quad \textbf{(6)}$$

In Eq.6, $f = 0.08$, is chosen such that the band limits of all the Mueller components fall within the radius = 0.1, of the Fourier domain filter. Processing the resulting single-shot intensity image $I(m,n)$ (Fig.3a), and using our equations defined in Table.1, we seamlessly recover all 16 Mueller matrix components. We compare the recovered Mueller matrix components with the original Mueller matrix components, pixel by pixel, by defining the error-metric as:

$$\text{Error}(m,n) = \sum_{i=1}^{4}\sum_{j=1}^{4} |M_{\text{obj},ij}(m,n) - M_{\text{recov},ij}(m,n)|. \quad \textbf{(7)}$$

As seen in Fig.3(b), the error is on the order of machine error ($1e^{-14}$), which means the recovered Mueller matrices exactly match the orginal Mueller matrices in the band-limited signal, as expected.

We also numerically test our method on an experimentally obtained Mueller matrix image. This particular example provides us with an interesting test case to simulate the performance of our method in a more practical setting. In this example, we image the Mueller matrix of a linear polarizer, which is experimentally obtained using DoT Mueller matrix imaging, by sequentially illuminating the linear polarizer with known polarization

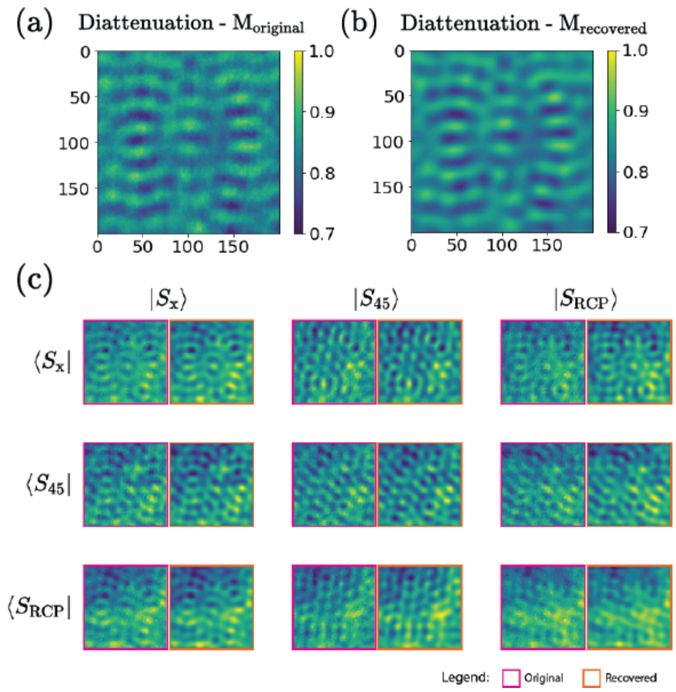

Fig. 4. Experimental Mueller Matrix Simulation Results. We numerically test our method on an experimentally obtained Mueller matrix image of a transmissive linear polarizer. **(a)** The diattenuation of the experimentally obtained Mueller matrix $\mathbf{M}_{\text{original}}$, as a function of spatial coordinates (m,n). **(b)** The diattenuation of the numerically recovered Mueller matrix $\mathbf{M}_{\text{original}}$, as a function of spatial coordinates (m,n). **(c)** Expectation values $\left\langle \vec{S}_\alpha \middle| \mathbf{M}(m,n) \middle| \vec{S}_\beta \right\rangle$ of both $\mathbf{M}_{\text{original}}$ and $\mathbf{M}_{\text{recovered}}$, calculated for different pairs of polarizations, and juxtaposed for comparison.

states, and then sequentially analyzing the fields by using polarization optics in front of a CCD sensor. We summarize the results in Fig.4. We plot the diattenuation [2] of the experimentally obtained Mueller matrix $\mathbf{M}_{\text{original}}$ in Fig.4(a), which, given we are imaging a linear polarizer, should ideally be exactly 1. Instead, we see it ranges from 0.7 - 1, with variation that can mainly be attributed to speckle. There are also some higher order spatial variations in Fig.4(a), that originate from the use of finite apertures in the beam path. After running a simulation of our technique on the experimentally obtained Mueller matrix image, we recover a Mueller matrix image $\mathbf{M}_{\text{recovered}}$ and plot its diattenutation as showed in Fig.4(b). We see that Fig.4(b) matches well with Fig.4(a), and faithfully recreates the low spatial frequency features seen in Fig.4(a), such as speckle. The much higher frequency features in Fig.4(a) are indeed missing in Fig.4(b), but that is to be expected given the low-pass filters applied in our technique around spatial frequency channels. We also plot the expectation values [2], as a function of spatial coordinates (m,n) of the Mueller matrices, defined as $\left\langle \vec{S}_\alpha \middle| \mathbf{M}(m,n) \middle| \vec{S}_\beta \right\rangle$, for a range of different polarization pairs, as shown in Fig.4(c). The expectation values for $\mathbf{M}_{\text{original}}$ and $\mathbf{M}_{\text{recovered}}$ are juxtaposed in Fig.4(c) for comparison. We see good correspondence between the original and recovered Mueller matrix images, and as expected, the lower frequency features are maintained. These images tell us that the Mueller matrix components themselves have been correctly recovered up to a certain error, introduced by the higher frequency terms.

In the experimental Mueller matrix image example, the predominant contribution to the spectrum is from the lower spatial frequencies, however, since the signal is not band-limited within the radius of our filters, it still presents an interesting test case example. Of course the viability of our technique would then depend upon application requirements, as imaging relatively high spatial frequency components could introduce significant aliasing, resulting in erroneous values for the recovered Mueller matrix image. Flexibility in the choice of filters used in the Fourier domain, could be one way to mitigate this shortcoming, based on the application. For instance, there may be applications in which the M_{00} component is swiftly varying in comparison to other components, and so then the Fourier filter at channel Xx can be chosen to be much larger in size, compared to neighboring filters. Thus, our design provides a practical pathway to implementing a simple, compact, snapshot Mueller matrix imaging system, especially in the context of low-spatial frequency imaging. The practical aspect of our design choices is also apparent in the form of our analyzer (1) and illumination (3) Stokes vectors. Both the analyzer and illumination vectors always maintain a degree of polarization (DOP) of 1, for any and all values of spatial frequency parameters a_A, b_A, a_I, b_I, and spatial coordinates (m, n). Creating precise structured illumination with spatially varying DOP is impractical at the moment, and similarly analyzing for a different DOP at each pixel of a Stokes-camera is also impractical. Our approach eliminates the concern of varying DOP, thus making a possible implementation with current technology, practically viable.

The main advantage of designing a compact, snapshot MMI device, is in MMI applications requiring real-time feedback and response. There are important biological and chemical sensing applications, that require compact, fast and real-time response in target detection, of certain cells or molecules, e.g. in the optical biopsy and functional characterization of biological tissues [17], identifying cancerous tissues from healthy tissues [18], and detection of chiral enantiomer molecules [19]. Additionally, there are emerging applications in computer vision, as well as material reconstruction, which could benefit from a compact snapshot MMI system. Compared to exisiting MMI methods, a system based on our design could be made to be compact by using only a single component (like a phase mask or metasurface [15, 16]) for illumination, and a DoFP sensor with an imaging optic. Furthermore, a compact, snapshot MMI system, given its short operation time and flexibility, could be useful in generating large MMI datasets for machine learning applications. This could possibly open up exciting new areas of investigation.

Table 1. Equations to compute elements. We summarize below the linear equations used to directly compute the Mueller matrix components from a single snap-shot intensity image $I(m, n)$. Θ operator signifies the circular low-pass filter applied in k-space, around spatial frequency channels given in the subscript. For example, Θ_{Xd} is the filter applied around channel Xd.

$M_{\_}$	Equation
M_{00}	$\mathcal{F}^{-1}\{\Theta_{Xx}(\mathcal{F}\{I(m,n)\})\}$
M_{01}	$\mathcal{F}^{-1}\{\Theta_{Xa}(\mathcal{F}\{I(m,n)\})+\Theta_{Xb}(\mathcal{F}\{I(m,n)\})+\Theta_{Xc}(\mathcal{F}\{I(m,n)\})+\Theta_{Xd}(\mathcal{F}\{I(m,n)\})\}$
M_{02}	$\mathcal{F}^{-1}\{\Theta_{Xa}(i\mathcal{F}\{I(m,n)\})-\Theta_{Xb}(i\mathcal{F}\{I(m,n)\})+\Theta_{Xc}(i\mathcal{F}\{I(m,n)\})-\Theta_{Xd}(i\mathcal{F}\{I(m,n)\})\}$
M_{03}	$\mathcal{F}^{-1}\{\Theta_{Xy}(i\mathcal{F}\{I(m,n)\})-\Theta_{Xz}(i\mathcal{F}\{I(m,n)\})\}$
M_{10}	$\mathcal{F}^{-1}\{\Theta_{Ax}(\mathcal{F}\{I(m,n)\})+\Theta_{Bx}(\mathcal{F}\{I(m,n)\})+\Theta_{Cx}(\mathcal{F}\{I(m,n)\})+\Theta_{Dx}(\mathcal{F}\{I(m,n)\})\}$
M_{11}	$\mathcal{F}^{-1}\{\Theta_{Aa}(\mathcal{F}\{I(m,n)\})+\Theta_{Ab}(\mathcal{F}\{I(m,n)\})+\Theta_{Ac}(\mathcal{F}\{I(m,n)\})+\Theta_{Ad}(\mathcal{F}\{I(m,n)\})+\Theta_{Ba}(\mathcal{F}\{I(m,n)\})+\Theta_{Bb}(\mathcal{F}\{I(m,n)\})+\Theta_{Bc}(\mathcal{F}\{I(m,n)\})+\Theta_{Bd}(\mathcal{F}\{I(m,n)\})+\Theta_{Ca}(\mathcal{F}\{I(m,n)\})+\Theta_{Cb}(\mathcal{F}\{I(m,n)\})+\Theta_{Cc}(\mathcal{F}\{I(m,n)\})+\Theta_{Cd}(\mathcal{F}\{I(m,n)\})+\Theta_{Da}(\mathcal{F}\{I(m,n)\})+\Theta_{Db}(\mathcal{F}\{I(m,n)\})+\Theta_{Dc}(\mathcal{F}\{I(m,n)\})+\Theta_{Dd}(\mathcal{F}\{I(m,n)\})\}$
M_{12}	$\mathcal{F}^{-1}\{\Theta_{Aa}(i\mathcal{F}\{I(m,n)\})-\Theta_{Ab}(i\mathcal{F}\{I(m,n)\})+\Theta_{Ac}(i\mathcal{F}\{I(m,n)\})-\Theta_{Ad}(i\mathcal{F}\{I(m,n)\})+\Theta_{Ba}(i\mathcal{F}\{I(m,n)\})-\Theta_{Bb}(i\mathcal{F}\{I(m,n)\})+\Theta_{Bc}(i\mathcal{F}\{I(m,n)\})-\Theta_{Bd}(i\mathcal{F}\{I(m,n)\})+\Theta_{Ca}(i\mathcal{F}\{I(m,n)\})-\Theta_{Cb}(i\mathcal{F}\{I(m,n)\})+\Theta_{Cc}(i\mathcal{F}\{I(m,n)\})-\Theta_{Cd}(i\mathcal{F}\{I(m,n)\})+\Theta_{Da}(i\mathcal{F}\{I(m,n)\})-\Theta_{Db}(i\mathcal{F}\{I(m,n)\})+\Theta_{Dc}(i\mathcal{F}\{I(m,n)\})-\Theta_{Dd}(i\mathcal{F}\{I(m,n)\})\}$
M_{13}	$\mathcal{F}^{-1}\{\Theta_{Ay}(i\mathcal{F}\{I(m,n)\})-\Theta_{Az}(i\mathcal{F}\{I(m,n)\})+\Theta_{By}(i\mathcal{F}\{I(m,n)\})-\Theta_{Bz}(i\mathcal{F}\{I(m,n)\})+\Theta_{Cy}(i\mathcal{F}\{I(m,n)\})-\Theta_{Cz}(i\mathcal{F}\{I(m,n)\})+\Theta_{Dy}(i\mathcal{F}\{I(m,n)\})-\Theta_{Dz}(i\mathcal{F}\{I(m,n)\})\}$
M_{20}	$\mathcal{F}^{-1}\{\Theta_{Ax}(i\mathcal{F}\{I(m,n)\})-\Theta_{Bx}(i\mathcal{F}\{I(m,n)\})+\Theta_{Cx}(i\mathcal{F}\{I(m,n)\})-\Theta_{Dx}(i\mathcal{F}\{I(m,n)\})\}$
M_{21}	$\mathcal{F}^{-1}\{\Theta_{Aa}(i\mathcal{F}\{I(m,n)\})+\Theta_{Ab}(i\mathcal{F}\{I(m,n)\})+\Theta_{Ac}(i\mathcal{F}\{I(m,n)\})+\Theta_{Ad}(i\mathcal{F}\{I(m,n)\})-\Theta_{Ba}(i\mathcal{F}\{I(m,n)\})-\Theta_{Bb}(i\mathcal{F}\{I(m,n)\})-\Theta_{Bc}(i\mathcal{F}\{I(m,n)\})-\Theta_{Bd}(i\mathcal{F}\{I(m,n)\})+\Theta_{Ca}(i\mathcal{F}\{I(m,n)\})+\Theta_{Cb}(i\mathcal{F}\{I(m,n)\})+\Theta_{Cc}(i\mathcal{F}\{I(m,n)\})+\Theta_{Cd}(i\mathcal{F}\{I(m,n)\})-\Theta_{Da}(i\mathcal{F}\{I(m,n)\})-\Theta_{Db}(i\mathcal{F}\{I(m,n)\})-\Theta_{Dc}(\mathcal{F}\{I(m,n)\})-\Theta_{Dd}(i\mathcal{F}\{I(m,n)\})\}$
M_{22}	$\mathcal{F}^{-1}\{-\Theta_{Aa}(\mathcal{F}\{I(m,n)\})+\Theta_{Ab}(\mathcal{F}\{I(m,n)\})-\Theta_{Ac}(\mathcal{F}\{I(m,n)\})+\Theta_{Ad}(\mathcal{F}\{I(m,n)\})+\Theta_{Ba}(\mathcal{F}\{I(m,n)\})-\Theta_{Bb}(\mathcal{F}\{I(m,n)\})+\Theta_{Bc}(\mathcal{F}\{I(m,n)\})-\Theta_{Bd}(\mathcal{F}\{I(m,n)\})-\Theta_{Ca}(\mathcal{F}\{I(m,n)\})+\Theta_{Cb}(\mathcal{F}\{I(m,n)\})-\Theta_{Cc}(\mathcal{F}\{I(m,n)\})+\Theta_{Cd}(\mathcal{F}\{I(m,n)\})+\Theta_{Da}(\mathcal{F}\{I(m,n)\})-\Theta_{Db}(\mathcal{F}\{I(m,n)\})+\Theta_{Dc}(\mathcal{F}\{I(m,n)\})-\Theta_{Dd}(\mathcal{F}\{I(m,n)\})\}$
M_{23}	$\mathcal{F}^{-1}\{-\Theta_{Ay}(\mathcal{F}\{I(m,n)\})+\Theta_{Az}(\mathcal{F}\{I(m,n)\})+\Theta_{By}(\mathcal{F}\{I(m,n)\})-\Theta_{Bz}(\mathcal{F}\{I(m,n)\})-\Theta_{Cy}(\mathcal{F}\{I(m,n)\})+\Theta_{Cz}(\mathcal{F}\{I(m,n)\})+\Theta_{Dy}(\mathcal{F}\{I(m,n)\})-\Theta_{Dz}(\mathcal{F}\{I(m,n)\})\}$
M_{30}	$\mathcal{F}^{-1}\{\Theta_{Yx}(i\mathcal{F}\{I(m,n)\})-\Theta_{Zx}(i\mathcal{F}\{I(m,n)\})\}$
M_{31}	$\mathcal{F}^{-1}\{\Theta_{Ya}(i\mathcal{F}\{I(m,n)\})+\Theta_{Yb}(i\mathcal{F}\{I(m,n)\})+\Theta_{Yc}(i\mathcal{F}\{I(m,n)\})+\Theta_{Yd}(i\mathcal{F}\{I(m,n)\})-\Theta_{Za}(i\mathcal{F}\{I(m,n)\})-\Theta_{Zb}(i\mathcal{F}\{I(m,n)\})-\Theta_{Zc}(i\mathcal{F}\{I(m,n)\})-\Theta_{Zd}(i\mathcal{F}\{I(m,n)\})\}$
M_{32}	$\mathcal{F}^{-1}\{-\Theta_{Ya}(\mathcal{F}\{I(m,n)\})+\Theta_{Yb}(\mathcal{F}\{I(m,n)\})-\Theta_{Yc}(\mathcal{F}\{I(m,n)\})+\Theta_{Yd}(\mathcal{F}\{I(m,n)\})+\Theta_{Za}(\mathcal{F}\{I(m,n)\})-\Theta_{Zb}(\mathcal{F}\{I(m,n)\})+\Theta_{Zc}(\mathcal{F}\{I(m,n)\})-\Theta_{Zd}(\mathcal{F}\{I(m,n)\})\}$
M_{33}	$\mathcal{F}^{-1}\{-\Theta_{Yy}(\mathcal{F}\{I(m,n)\})+\Theta_{Yz}(\mathcal{F}\{I(m,n)\})+\Theta_{Zy}(\mathcal{F}\{I(m,n)\})-\Theta_{Zz}(\mathcal{F}\{I(m,n)\})\}$

Disclosure

The authors declare no competing interests.

Data availability

Data may be obtained from the authors upon reasonable request.

REFERENCES

1. R. A. Chipman, E. A. Sornsin, and J. L. Pezzaniti, in *International Symposium on Polarization Analysis and Applications to Device Technology,* T. Yoshizawa and H. Yokota, eds. (SPIE, 1996).
2. R. A. Chipman, W.-S. T. Lam, and G. Young, *Polarized Light and Optical Systems* (CRC Press, 2018).
3. J. L. Pezzaniti, Opt. Eng. **34**, 1558 (1995).
4. I. Berezhnyy and A. Dogariu, Opt. Express **12**, 4635 (2004).
5. I. J. Vaughn, O. G. Rodríguez-Herrera, M. Xu, and J. S. Tyo, in *Polarization Science and Remote Sensing VII,* J. A. Shaw and D. A. LeMaster, eds. (SPIE, 2015).
6. M. Gonzalez, K. A. Montejo, K. Krupp, V. Srinivas, E. DeHoog, P. Madhivanan, and J. C. Ramella-Roman, J. Biomed. Opt. **25** (2020).
7. M. W. Kudenov, M. J. Escuti, N. Hagen, E. L. Dereniak, and K. Oka, Opt. Lett. **37**, 1367 (2012).
8. Y. Wang, M. Kudenov, A. Kashani, J. Schwiegerling, and M. Escuti, in *Polarization Science and Remote Sensing VII,* J. A. Shaw and D. A. LeMaster, eds. (SPIE, 2015).
9. C. S. L. Chun, D. L. Fleming, and E. J. Torok, in *Automatic Object Recognition IV,* F. A. Sadjadi, ed. (SPIE, 1994).
10. D. J. Phillips, A.-M. Dorsett, and G. A. Finney, in *Airborne Intelligence, Surveillance, Reconnaissance (ISR) Systems and Applications VI,* D. J. Henry, ed. (SPIE, 2009).
11. J. S. Tyo, C. F. LaCasse, and B. M. Ratliff, Opt. Lett. **34**, 3187 (2009).
12. J. S. Tyo, D. L. Goldstein, D. B. Chenault, and J. A. Shaw, Appl. Opt. **45**, 5453 (2006).
13. G. Myhre, W.-L. Hsu, A. Peinado, C. LaCasse, N. Brock, R. A. Chipman, and S. Pau, Opt. Express **20**, 27393 (2012).
14. A. S. Alenin, I. J. Vaughn, and J. S. Tyo, Appl. Opt. **57**, 2327 (2018).
15. E. Arbabi, S. M. Kamali, A. Arbabi, and A. Faraon, ACS Photonics **6**, 2712 (2019).
16. N. A. Rubin, A. Zaidi, A. H. Dorrah, Z. Shi, and F. Capasso, Sci. Adv. **7**, eabg7488 (2021).
17. L. Trifonyuk, A. Sdobnov, W. Baranowski, V. Ushenko, O. Olar, A. Dubolazov, L. Pidkamin, M. Sidor, O. Vanchuliak, A. Motrich, M. Gorsky, and I. Meglinski, Lasers Med. Sci. **35**, 877 (2019).
18. S. K. U., K. K. Mahato, and N. Mazumder, Lasers Med. Sci. **34**, 1283 (2019).
19. Y. Zhao, A. N. Askarpour, L. Sun, J. Shi, X. Li, and A. Alù, Nat. Commun. **8** (2017).

FULL REFERENCES

1. R. A. Chipman, E. A. Sornsin, and J. L. Pezzaniti, in *International Symposium on Polarization Analysis and Applications to Device Technology,* T. Yoshizawa and H. Yokota, eds. (SPIE, 1996).
2. R. A. Chipman, W.-S. T. Lam, and G. Young, *Polarized Light and Optical Systems* (CRC Press, 2018).
3. J. L. Pezzaniti, "Mueller matrix imaging polarimetry," Opt. Eng. **34**, 1558 (1995).
4. I. Berezhnyy and A. Dogariu, "Time-resolved mueller matrix imaging polarimetry," Opt. Express **12**, 4635 (2004).
5. I. J. Vaughn, O. G. Rodríguez-Herrera, M. Xu, and J. S. Tyo, in *Polarization Science and Remote Sensing VII,* J. A. Shaw and D. A. LeMaster, eds. (SPIE, 2015).
6. M. Gonzalez, K. A. Montejo, K. Krupp, V. Srinivas, E. DeHoog, P. Madhivanan, and J. C. Ramella-Roman, "Design and implementation of a portable colposcope mueller matrix polarimeter," J. Biomed. Opt. **25** (2020).
7. M. W. Kudenov, M. J. Escuti, N. Hagen, E. L. Dereniak, and K. Oka, "Snapshot imaging mueller matrix polarimeter using polarization gratings," Opt. Lett. **37**, 1367 (2012).
8. Y. Wang, M. Kudenov, A. Kashani, J. Schwiegerling, and M. Escuti, in *Polarization Science and Remote Sensing VII,* J. A. Shaw and D. A. LeMaster, eds. (SPIE, 2015).
9. C. S. L. Chun, D. L. Fleming, and E. J. Torok, in *Automatic Object Recognition IV,* F. A. Sadjadi, ed. (SPIE, 1994).
10. D. J. Phillips, A.-M. Dorsett, and G. A. Finney, in *Airborne Intelligence, Surveillance, Reconnaissance (ISR) Systems and Applications VI,* D. J. Henry, ed. (SPIE, 2009).
11. J. S. Tyo, C. F. LaCasse, and B. M. Ratliff, "Total elimination of sampling errors in polarization imagery obtained with integrated microgrid polarimeters," Opt. Lett. **34**, 3187 (2009).
12. J. S. Tyo, D. L. Goldstein, D. B. Chenault, and J. A. Shaw, "Review of passive imaging polarimetry for remote sensing applications," Appl. Opt. **45**, 5453 (2006).
13. G. Myhre, W.-L. Hsu, A. Peinado, C. LaCasse, N. Brock, R. A. Chipman, and S. Pau, "Liquid crystal polymer full-stokes division of focal plane polarimeter," Opt. Express **20**, 27393 (2012).
14. A. S. Alenin, I. J. Vaughn, and J. S. Tyo, "Optimal bandwidth and systematic error of full-stokes micropolarizer arrays," Appl. Opt. **57**, 2327 (2018).
15. E. Arbabi, S. M. Kamali, A. Arbabi, and A. Faraon, "Vectorial holograms with a dielectric metasurface: Ultimate polarization pattern generation," ACS Photonics **6**, 2712–2718 (2019).
16. N. A. Rubin, A. Zaidi, A. H. Dorrah, Z. Shi, and F. Capasso, "Jones matrix holography with metasurfaces," Sci. Adv. **7**, eabg7488 (2021).
17. L. Trifonyuk, A. Sdobnov, W. Baranowski, V. Ushenko, O. Olar, A. Dubolazov, L. Pidkamin, M. Sidor, O. Vanchuliak, A. Motrich, M. Gorsky, and I. Meglinski, "Differential mueller matrix imaging of partially depolarizing optically anisotropic biological tissues," Lasers Med. Sci. **35**, 877–891 (2019).
18. S. K. U., K. K. Mahato, and N. Mazumder, "Polarization-resolved stokes-mueller imaging: a review of technology and applications," Lasers Med. Sci. **34**, 1283–1293 (2019).
19. Y. Zhao, A. N. Askarpour, L. Sun, J. Shi, X. Li, and A. Alù, "Chirality detection of enantiomers using twisted optical metamaterials," Nat. Commun. **8** (2017).